CATALYSIS

Sabatier principle of metal-support interaction for design of ultrastable metal nanocatalysts

Sulei Hu and Wei-Xue Li*

The stability of supported nanocatalysts is crucial to meeting environmental and energy challenges and necessitates fundamental theory to relieve trial-and-error experimentation and accelerate lab-to-fab translation. Here, we report a Sabatier principle of metal-support interaction for stabilizing metal nanocatalysts against sintering based on the kinetic simulations of 323 metal-support pairs using scaling relations from 1252 energetics data. Too strong of an interaction is shown to trigger Ostwald ripening, whereas too weak of an interaction stimulates particle migration and coalescence. High-throughput screening of supports enables the sintering resistance of nanocatalysts to reach the Tammann temperature on homogeneous supports and far beyond it on heteroenergetic supports. This theory, which is substantiated by first-principles neural network molecular dynamics simulations and experiments, paves the way for the design of ultrastable nanocatalysts.

The stability of nanomaterials is a matter of life(time) and death in various nano-technologies, especially for heterogeneous metal nanocatalysts, to meet energy and environmental requirements (1). The instability, among other issues, caused by the thermal- and/or chemical-induced sintering (2) of smaller metal nanoparticles (NPs) into larger NPs with shrinking atomic utilization severely decreases productivity, delays the lab-to-fab translation of highly active nanocatalysts (3), and requires plant shutdown for catalyst replacement or regeneration with large capital costs (4). The rational design of nanocatalysts with sufficient thermal resistance and operando lifetime, in addition to high activity and selectivity, has important economic and scientific value, even for the general nanoscience field (5).

Sintering of metal NPs proceeds through the formation and diffusion of metal atoms and/or metal-reactant complexes [Ostwald ripening (OR)] (6, 7) and/or through particle migration and coalescence (PMC) on the support (Fig. 1A) (8). To mitigate sintering, physical approaches such as spatial confinement and geometric shielding (9) have been used, which involve the incorporation of NPs into one-dimensional (1D) tubular or 3D micro- or mesoporous materials (10) and the full or partial encapsulation of NPs with less-reactive thin films with microchannels (11). The cost of these approaches is the blockage of active sites and the impeded transport of reactants. Chemically, alteration of metal-support interaction (MSI) is used to stabilize NPs and control the

sintering kinetics (12), which is, however, a complex function of the support composition and surface orientation and defects (13), interface structure, lattice mismatch, mixing and alloy phase formation, charge rearrangement (14), and reaction conditions (15). This fact results in a large gap between the sintering kinetics and the underlying MSI and challenges the screening and/or optimization of supports, thereby necessitating expensive trial-and-error experimentation (3). To bridge this gap, it is vital to identify the corresponding MSI descriptor and determine the governing rule for the sintering kinetics and develop a design theory to engineer the metal-support interface for ultrastable nanocatalysts.

Here, we report a Sabatier principle of MSI for the stability of supported metal NPs against sintering based on the linear scaling relationship between the particle adhesion energy and atom binding energy with supports, two MSI descriptors for the corresponding OR and PMC processes. Sintering kinetic simulations of 10 transition metals (TMs) and 91 supports (323 metal-support pairs in total) using 1252 energetics data were conducted, and a universal volcanic dependence of the sintering kinetics on MSI was revealed. It was found that the optimal MSI corresponding to the highest stability on homogeneous supports should be neither too strong nor too weak. Too strong of a MSI triggered rapid OR, whereas too weak of a MSI stimulated facile PMC, both of which severely worsened the stability. For supports with the optimal MSI to NPs, the sintering onset temperature is about half of the melting temperature T_m of the bulk metal for typical NPs (~3 nm), substantiated by the long-reported empirical Tammann temperature. The revealed Sabatier principle enables the high-throughput screening of heteroenergetic supports to break the scaling relationship and boost the sintering resistance of the supported NPs far beyond the Tammann

temperature. This theory, which is substantiated by molecular dynamics (MD) simulations based on the first-principles neural network potential (16) and available experiments (17), paves the way for the design of ultrastable nanocatalysts.

Scaling relationships

The size growth rate of NPs through OR is determined by the total activation energy E_{act} (OR) = $E_{bs} - E_c + E_{ds}$ describing the formation ($E_{bs} - E_c$) of the ripening monomer (herein metal atom) with respect to the cohesive energy E_c (negative) of bulk metal and its diffusion on the support (18). Both the binding energy E_{bs} (negative) and diffusion barrier E_{ds} (positive) of the metal atom on the support depend on the MSI. To identify the appropriate MSI descriptor, we retrieved 32 TM atoms and 61 supports (292 metal-support pairs in total) from the literature [see supplementary materials (SM) and data S1 to S6], including various pristine oxide compounds, TMs, and thin films, whose E_{bs} and E_{ds} were calculated using density functional theory (DFT). For most of the considered surfaces, especially corrugated oxides and TM surfaces, E_{ds} falls statistically in a region exhibiting a linear scaling relation with E_{bs}, that is, $E_{ds} = k_{ds}E_{bs}$ [slope (k_{ds}) = –0.18, coefficient of determination (R^2) = 0.86] (green region in Fig. 1B). Note that the flat surfaces that fall statistically in the purple region have a smaller slope. The results could be rationalized by the fact that the diffusion barrier E_{ds} of the metal atom is proportional to its binding strength E_{bs}, with a slope determined by, among other features, the surface corrugation (see SM for more details). This relationship simplifies the activation energy as

$$E_{act}(OR) = kE_{bs} - E_c \qquad (1)$$

where $k = 0.82$ and E_{bs} is used as the MSI descriptor for the OR kinetics below.

The size growth rate of NPs through PMC is determined by the particle diffusion barrier $E_{act}(PMC) = E_{act}^m - S^m E_{adh}$ consisting of the self-activation energy E_{act}^m of the metal atom on the metal particle surface and the cost of the particle adhesion energy E_{adh} (negative) to the support (where S^m is the area per atom) (19, 20). E_{act}^m was found to be proportional to the corresponding E_c (fig. S1), $E_{act}^m = -0.33E_c$ ($R^2 = 0.95$), based on the DFT values from more than 200 TM pristine surfaces retrieved from the literature (SM and data S1). Thus, the particle diffusion barrier becomes

$$E_{act}(PMC) = -S^m E_{adh} - 0.33 E_c \qquad (2)$$

where E_{adh} as the MSI descriptor for PMC can be calculated by DFT or experimentally extracted. We retrieved the measured contact

Hefei National Laboratory for Physical Sciences at the Microscale, School of Chemistry and Materials Science, Key Laboratory of Surface and Interface Chemistry and Energy Catalysis of Anhui Higher Education Institutes, iChEM, University of Science and Technology of China, Hefei, China.
*Corresponding author. Email: wxli70@ustc.edu.cn
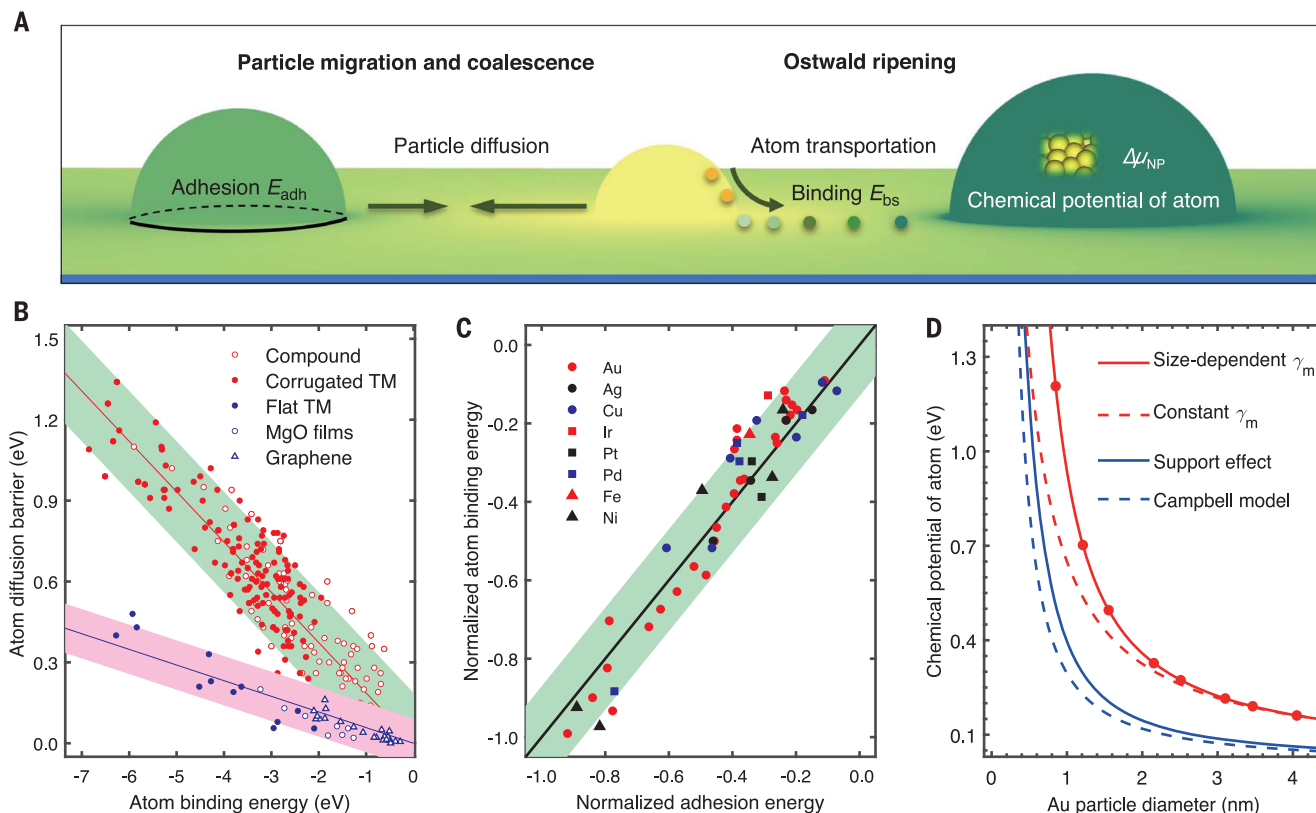
Fig. 1. Sintering mechanism and scaling relations for the energetics.
(**A**) Schematic of PMC and OR of supported metal NPs. (**B**) The diffusion barrier E_{ds} and binding energy E_{bs} of metal atoms on corrugated surfaces, including oxide compounds (red open circles) and TMs (red solid circles) in the green region, and on flat surfaces including TM(111) (blue solid circles), MgO films (blue open circles), and graphene on metal (blue open triangles) in the purple region (SM and data S1). The colored regions indicate the distribution range of the data. (**C**) Metal particle adhesion energy E_{adh} (normalized by two times the surface energy γ_m of the bulk metal) versus metal atom binding energy E_{bs} (normalized by the metal bulk cohesive energy E_c) (data S3). The colored region indicates the distribution range of the data. (**D**) Chemical potential $\Delta\mu_{NP}$ of the atoms in unsupported spherical NPs under constant (red dashed line) and size-dependent (red solid line) γ_m values and $\Delta\mu_{NP}$ value for CeO_{2-x}-supported Au NPs with a contact angle of 43° (blue solid line) and that based on Campbell's model (*23*) (blue dashed line) as a function of the diameter of the unsupported spherical NPs.

angle α of 188 metal-support pairs, including 10 late TMs from the literature (data S2), and calculated the corresponding E_{adh} using Young-Dupre's equation and the experimental surface energy of bulk metal. Depending on the metal-support pairs, E_{adh} varied at a wide range of values from –23 to –327 meV/Å², though the calorimetric experiments showed that E_{adh} is sensitive to the cleanliness of the surface (*21*).

For a given metal-support pair, the corresponding E_{bs} and E_{adh} are highly correlated. To figure out the correlation, we constructed a series of Ag-supported MgO(100) films (*22*) with thicknesses from 1 to 8 monolayers (fig. S2) and calculated their E_{bs} and E_{adh} toward the Au atom and film using DFT (data S3), respectively. Both values decreased with the film thickness and exhibited a linear scaling relationship, $S^m E_{adh} \cong E_{bs}/3$ ($R^2 = 0.94$) (fig. S3A). Moreover, we considered another 42 metal-support pairs retrieved from the literature, and the corresponding E_{adh} from experiments and E_{bs} from DFT were both available

(data S3), from which nearly the same relation as above was found (fig. S3B). To rationalize the results, we note that a given support adhering strongly to a metal particle would be strongly bound to the metal atom, and the energy gain for the adhesion (per atom) of the particle with a larger coordination is smaller than that of the metal atom to the support. Note that for the bulk metals themselves, there are two relevant quantities with E_{bs} and E_{adh}, that is, the cohesive energy E_c and surface energy γ_m. These two quantities were found to follow a similar scaling relationship, $2S^m\gamma_m \cong -1/3E_c$ (fig. S4). Normalizing the previous relationship by the latter one, a dimensionless scaling relationship

$$E_{adh}/2\gamma_m = -E_{bs}/E_c \qquad (3)$$

was introduced ($R^2 = 0.89$; see SM for more details), and a diagonal line crossing the origin is depicted in Fig. 1C. For the metal-support pair of interest, when either E_{adh} or E_{bs} was

available, Eq. 3 was applied to estimate the unavailable one (fig. S5). With these paired E_{adh} and E_{bs} values, $E_{act}(OR)$ and $E_{act}(PMC)$ were calculated for the kinetic simulation below (figs. S6 and S7).

The chemical potential $\Delta\mu_{NP}$ of metal atoms in NPs with respect to the bulk metal is crucial for the rate of both OR and PMC. According to the Gibbs-Thomson equation, $\Delta\mu_{NP}$ is proportional to the γ_m of the metal NPs, whose value differs from the bulk value at small size owing to the increased ratio of the lower-coordinated atoms exposed. The change in the surface coordination was estimated by counting various constructed Wulff-shaped NPs of different sizes (fig. S8), and, based on this, a size-dependent γ_m was established (fig. S9). For a NP with a given volume on different supports, different E_{adh} leads to different α and radius R of curvature, and the corresponding $\Delta\mu_{NP}$ becomes support-dependent throughout this work (see SM for more details). Using CeO_{2-x}-supported Au NPs as an example, the resulting $\Delta\mu_{NP}$ values (blue solid line) in Fig. 1D were notably
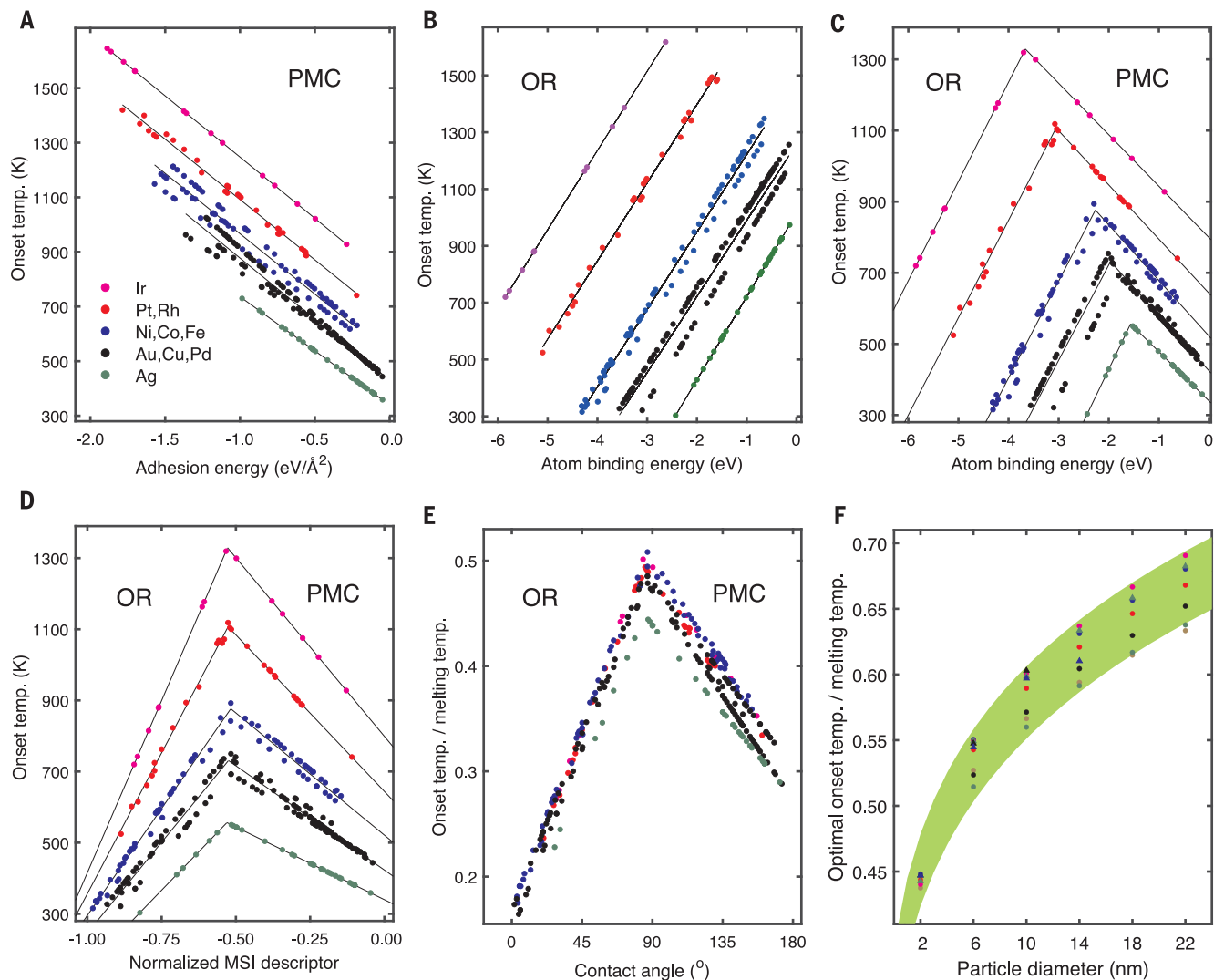
Fig. 2. Volcanic curves of the stability of NPs as a function of MSI.
(**A**) Calculated onset temperature T_{on} through PMC versus the metal particle adhesion energy $S^m E_{adh}$ during temperature-programmed kinetics at a heating rate of 1 K/s. On each support, the NPs had the same volume as that of the unsupported spherical NPs with an average diameter of 3.0 ± 0.30 nm. (**B**) T_{on} through OR versus the metal atom binding energy E_{bs}. (**C**) Sintering T_{on}, corresponding to the lower T_{on} between PMC and OR, versus E_{bs}. (**D**) Sintering T_{on} versus the normalized MSI descriptors of $E_{adh}/2\gamma_m$ or $-E_{bs}/E_c$. (**E**) Sintering T_{on} normalized by the melting temperature T_m of the bulk metal versus the contact angle. (**F**) Peak T_{on} normalized by T_m versus the initial average diameter. The shaded region indicates the distribution range of the data. All the data are listed in the SM. Sensitivity analysis of the scaling relationships used and the impact of their uncertainties on the volcanic curves and trend behavior can be found in the SM.

lower than those of the unsupported NPs (red solid line), consistent with Campbell's model (blue dashed line) (23).

### Sintering volcano on homogeneous supports

We now turn to the temperature-programmed OR and PMC kinetic simulations of the above 323 metal-support pairs with the same typical initial average diameter of 3.0 ± 0.3 nm (spherical NPs before contact with the supports of interest). During heating, the onset temperature T_{on} corresponding to a 10% decrease in particle number is defined to estimate the thermal resistance against PMC and

OR (methodology details in the SM). The simulated T_{on} for PMC was found to linearly increase with the absolute value of $S^m E_{adh}$ (Fig. 2A and fig. S10). Depending on the TMs, the enhanced MSI strength improves the thermal resistance to PMC by 400 to 700 K owing to the increase of E_{act}(PMC) (fig. S7). Consistently, the diffusion coefficient of the supported NPs decreases by five to six orders of magnitude (fig. S11). By contrast, the simulated T_{on} for OR linearly decreased with the absolute value of E_{bs}, as shown in Fig. 2B and fig. S12. This trend was observed because E_{act} (OR) decreased with the MSI strength (fig.

S6), and the thermal resistance to OR weakened accordingly.

Because both the OR and PMC contribute to the sintering, the effective T_{on} for the overall sintering is determined by the faster one with the lower T_{on}. Considering the counter-dependence of the OR and PMC rate on MSI and the constraint of the scaling relationship between E_{adh} and E_{bs} (Eq. 3), a volcanic dependence of the effective T_{on} was immediately seen and plotted in Fig. 2C and fig. S13 with respect to E_{bs} or $S^m E_{adh}$, respectively. At the left side of the volcanic peak where the corresponding MSI was strong, OR had a lower
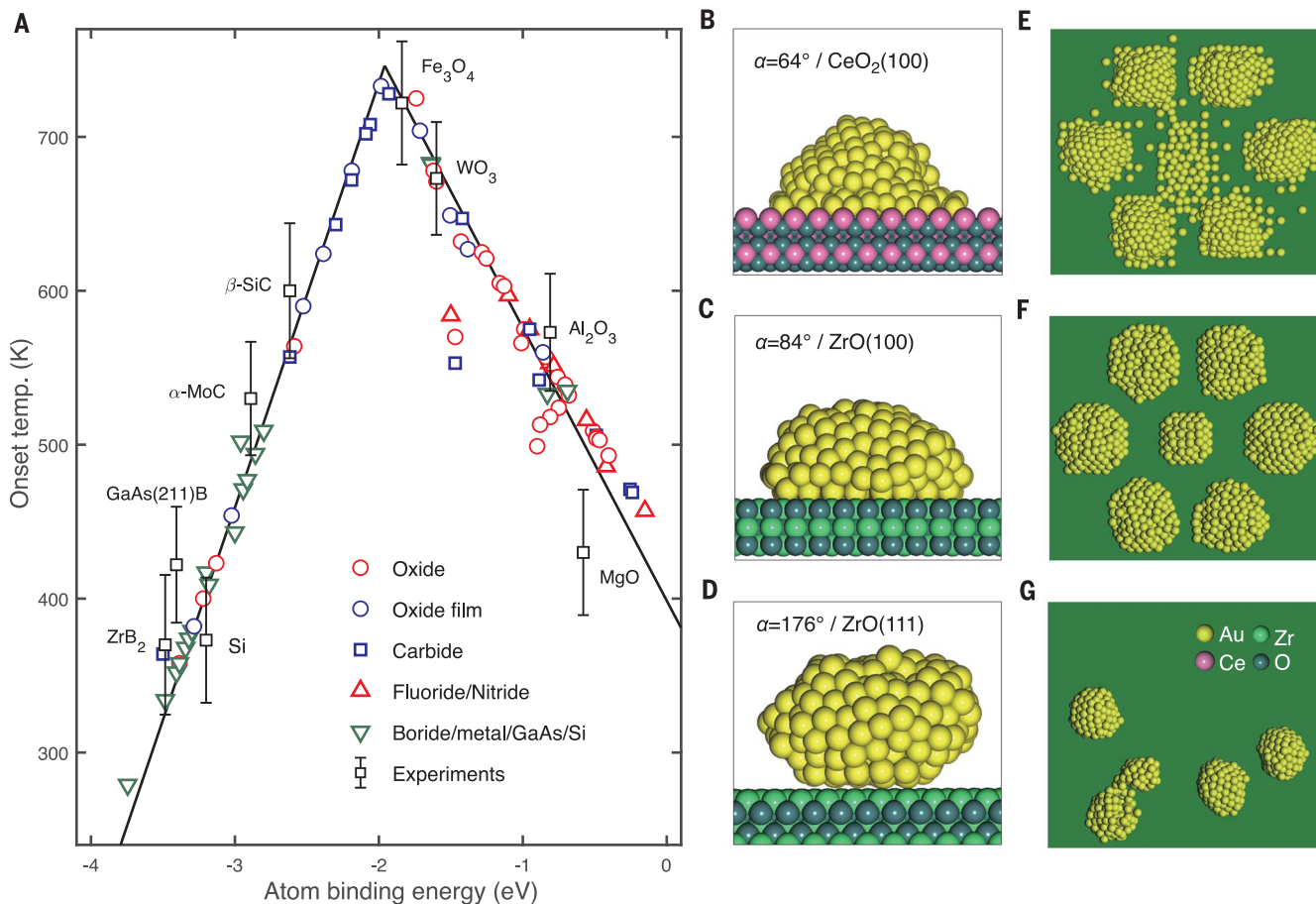
Fig. 3. Volcanic curves of supported Au NPs and MD simulations.
(**A**) Calculated onset temperature of Au NPs (3 nm) versus Au atom binding energy onto various supports. The black squares indicate the experimental values with error bars of ±46 K based on the uncertainty in the size distribution and loading (data S4). The error bars indicate the uncertainty of the experimental temperature. (**B** to **G**) MD snapshots using the first-principle neural network potential at 800 K at 10^5 time steps of 1 fs for one Au_{299} cluster [(B) to (D)] and seven Au clusters (one Au_{69} and six Au_{157}) [(E) to (G)] on Ce-terminated $CeO_2(100)$ [(B) and (E)], Zr-terminated $ZrO(100)$ [(C) and (F)], and Zr-terminated $ZrO(111)$ [(D) and (G)].

T_{on} and faster rate than PMC, irrespective of the TMs considered. On the right side with weak MSI, PMC had a lower T_{on} and dominated the sintering process. At the volcanic peak with the optimal MSI (neither too strong nor too weak), the rates of OR and PMC became balanced, but neither was facile. The optimum MSI and corresponding peak temperature showed a great dependence on the metal composition: The stronger the optimal MSI was (−3.73 eV for Ir versus −1.67 eV for Ag), the higher the peak T_{on} was (1330 versus 540 K). To unravel the underlying physics, we used the normalized descriptors of $E_{adh}/2\gamma_m$ or $-E_{bs}/E_c$ to replot Fig. 2C. The optimal MSI after normalization became insensitive to the composition and approximated to a constant value of −0.53 (Fig. 2D). The constant optimal MSI could be derived approximately by setting $E_{act}(OR) = E_{act}(PMC)$ (fig. S14), highlighting the key role of the elementary activation in these two processes to the overall sintering.

The T_{on} value for each TM (Fig. 2D) was further normalized by the melting temperature T_m of the bulk metal counterparts and then replotted versus the corresponding α value using Young-Dupre's equation in Fig. 2E. All the volcanic curves were found to be nearly overlapping, with a peak T_{on} at $0.47T_m \pm 0.02T_m$. This overlap was not unexpected because both T_m and the peak T_{on} depended similarly on the E_c of the bulk metals (fig. S15). To see the size effect on the volcanic curves, we increased the initial average diameter of the unsupported NPs from 2 to 22 nm. The optimal MSI was not found to be affected by particle size (fig. S16). However, the peak T_{on} for these 10 TMs increased from $0.44T_m \pm 0.01T_m$ to $0.67T_m \pm 0.03T_m$ (Fig. 2F). These peak T_{on} values were substantiated by the Tammann temperature ($\sim 0.5T_m$) of the bulk metal counterparts as the long-reported feature that empirically characterized the sintering temperature of materials. Under reaction conditions, the reactant might stabilize the metal atoms to form metal-reactant complexes on the support (6), leading to a metal-reactant interaction–dependent volcanic curve, as discussed in the SM.

Sintering volcano for Au NPs on homogeneous supports

As proof of principle, the sintering of Au NPs that is sensitive to MSI (24) was investigated. The calculated T_{on} values over 82 pristine surfaces were plotted versus the corresponding E_{bs} values in Fig. 3A. Ionic compounds, including oxides, fluorides, and nitrides, attained a relatively weak MSI with Au and were mainly distributed on the right side of the volcanic curve. Carbides with noble metal features that bind modestly to Au were distributed on both sides. However, supports that were dominated by metallic or covalent bonds, such as metal, boride, semiconductor, or oxide films, exhibited a strong MSI with Au and were distributed mainly on the left side. Figure 3A also presents the available experimental data for comparison. Specifically, for MgO, Al_2O_3 and
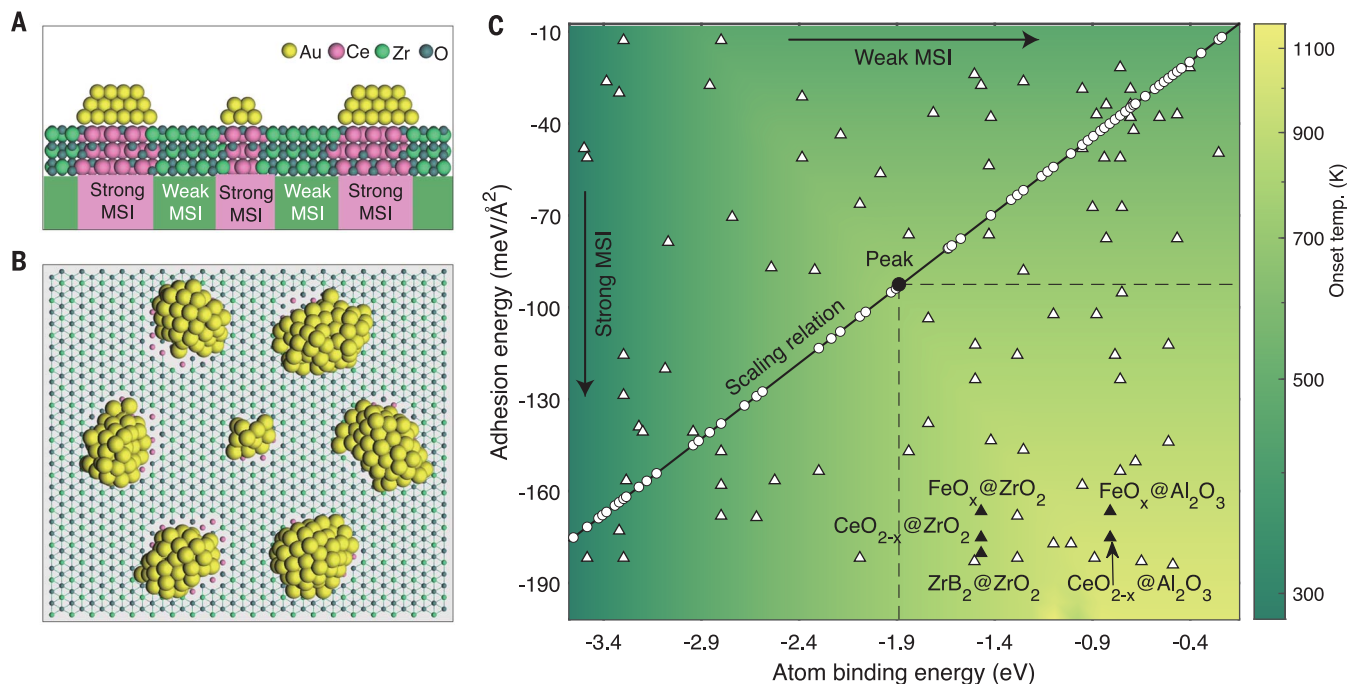
Fig. 4. Screening of heteroenergetic supports beyond the volcanic curves. (**A**) Heteroenergetic support S@W [CeO$_{2-x}$/ZrO$_2$(111)] containing a small area of domains S (CeO$_{2-x}$) with large absolute E_{adh} to Au clusters surrounded by a large area of domains W (ZrO$_2$) with small absolute E_{bs} to Au atoms. The colored regions in Fig. 4A are just used to distinguish the space distribution of the domain S and domain W. (**B**) Snapshot of the MD simulation after 80 ps (800 K) for one Au$_{19}$ and six Au$_{55}$ clusters on the CeO$_{2-x}$ domains of CeO$_{2-x}$@ZrO$_2$(111). (**C**) Onset temperature of sintering of the Au NPs (3 nm) supported on the S domains of the S@W support versus the E_{adh} value (y axis) of the Au NPs onto S domains and the E_{bs} value (x axis) of the Au atoms onto W domains.

WO$_3$ located on the right side (fig. S17, A and B), sintering was experimentally observed to proceed through PMC, as predicted by the above kinetic theory. By contrast, for GaAs(211)B and ZrB$_2$ on the left side, sintering was observed to proceed through OR, also in agreement with the theory (fig. S17, C and D). Fe$_3$O$_4$(111) had the optimal MSI to Au and was predicted with a peak temperature of 743 K. Indeed, when annealing at a temperature of 773 K, scanning tunneling microscopy (STM) revealed simultaneous Au particle agglomeration and atom migration, suggesting that PMC and OR occurred at a comparable rate and that neither of them was facile (*25*). Consistent trends between theory and experiment were also found for industry-related Pt and Rh nanocatalysts (fig. S18). Moreover, data from STM experiments also showed a preferential OR process for Pd$_{19}$ clusters on Rh(111) with a strong metal-metal bond at the interface (*26*). The agreement with experiments substantiated the trend behavior and underlying mechanism revealed by the kinetic simulations.

The Sabatier principle was further supported by MD simulations using the first-principles neural network potential (*16*). Twelve oxide surfaces with different compositions and surface structures were constructed to cover a wide range of MSI to Au. (figs. S19 to S23)

One small Au$_{69}$ and six large Au$_{157}$ clusters were supported on the constructed surfaces (10 nm by 10 nm), and MD simulations were performed at 800 K for 100 ps. For Ce-terminated CeO$_2$(100) interacting strongly with Au at the left side ($\alpha = 64°$; Fig. 3B), MD simulations revealed detachment of Au atoms from the small Au$_{69}$ cluster and diffusion toward large Au$_{157}$ clusters and no cluster diffusion was observed during the simulation time (movie S1), indicating a typical OR feature. By contrast, for Zr-terminated ZrO(111) interacting weakly with Au ($\alpha = 176°$; Fig. 3D), the small Au$_{69}$ cluster diffused toward the large Au$_{157}$ cluster (Fig. 3G) and there was no atom detachment found, a typical feature involved in PMC (movie S3). For ZrO(100) near the optimal MSI ($\alpha = 84°$; Fig. 3C), neither atom detachment nor cluster migration was observed within the simulation time (Fig. 3F and movie S2), consistent with the volcanic peak exhibiting a higher stability against sintering.

Beyond Tammann temperature on bifunctional heteroenergetic supports

A further increase in thermal stability beyond the volcanic peak, which is crucial for subnanometer metal clusters and high-temperature catalytic reactions, necessitates breaking of the scaling relationship between E_{adh} and E_{bs}

(Eq. 3). This feature, among others, can be achieved by constructing a bifunctional hetero-energetic support S@W, where support S at the nanoscale with strong adhesion (large absolute E_{adh}) pins metal NPs to suppress PMC and support W with weak binding (small absolute E_{bs}) prevents the formation of metal atoms to inhibit OR. As an example, we constructed a heteroenergetic support of CeO$_{2-x}$@ZrO$_2$(111) (Fig. 4A), where CeO$_{2-x}$(111) domains containing 15% oxygen vacancies (*24*) adhering strongly with Au (fig. S24, A to D) were embedded into the matrix of ZrO$_2$(111) binding weakly with Au (fig. S24, E to H). Small Au$_{19}$ and six Au$_{55}$ clusters were deposited on separated CeO$_{2-x}$(111) domains with a size comparable to that of the Au clusters. On homogeneous ZrO(100) with optimal MSI as confirmed above (Fig. 3, C and F), MD simulation at 800 K indicated that these small clusters became unstable even at the beginning (fig. S25). However, on CeO$_{2-x}$@ZrO$_2$(111), neither cluster migration nor atom detachment from Au$_{19}$ were observed (Fig. 4B and movie S4). Note that a dual-oxide support was proposed to increase the diffusion barrier of metal NPs or atoms across the support surface (*2, 27*).

The revealed Sabatier principle and scaling relationships can enable the high-throughput screening of the heteroenergetic support S@W. For the Au NPs of ~3 nm in Fig. 3A, any two of

the 82 supports can be regarded as S and W domains in turn, generating 6724 combinations. For each combination, the lower T_{on} between that attributed to PMC on the S domains and that attributed to OR on the W domains determines the effective T_{on} of sintering. These T_{on} values yield a 2D sintering map with respect to E_{adh} for S (y axis) and E_{bs} for W (x axis) (Fig. 4C). The diagonal line from the bottom left to the top right corresponds to the volcanic curve in Fig. 3A with a peak T_{on} of 743 K. Notably, at the bottom right quarter of the 2D map that includes 1681 heteroenergetic supports with large $|E_{adh}|$ for S and small $|E_{bs}|$ for W, all the effective T_{on} exceeded 743 K and had a maximum even up to 1140 K (~$0.85T_m$). Among others, CeO$_{2-x}$@ZrO$_2$ and CeO$_{2-x}$@Al$_2$O$_3$ were predicted to appear in this area, and the effective T_{on} were 1050 and 1100 K, respectively. Because the support W that bound weakly with metal atoms is also reluctant to form the metal-reactant complexes, influence of reaction conditions on chemical stability of supported metal NPs through the reactant-promoted OR on the corresponding heteroenergetic S@W could be relieved (see SM for more details). Indeed, CeO$_{2-x}$@ZrO$_2$ as a crucial additive has been applied in commercial automotive exhaust catalysts to improve the overall stability under practical application (*28*). Highly durable three-way catalysts as small as a dozen atoms in size were realized on CeO$_{2-x}$@Al$_2$O$_3$ under severe hydrothermal aging conditions at 1173 K,

and the corresponding structure can maintain its stability for 24 hours (*17*). Considering that the new active sites might form at the boundaries between nanocatalyst and support, the heteroenergetic supports provide a platform to simultaneously improve the stability, activity, and selectivity of supported nanocatalysts.

REFERENCES AND NOTES

1. H. Chen *et al.*, *ACS Cent. Sci.* **6**, 1617–1627 (2020).
2. Y. Dai, P. Lu, Z. Cao, C. T. Campbell, Y. Xia, *Chem. Soc. Rev.* **47**, 4314–4331 (2018).
3. A. K. Datye, M. Votsmeier, *Nat. Mater.* **20**, 1049–1059 (2021).
4. M. Rahmati, M. S. Safdari, T. H. Fletcher, M. D. Argyle, C. H. Bartholomew, *Chem. Rev.* **120**, 4455–4533 (2020).
5. S. L. Scott, *ACS Catal.* **8**, 8597–8599 (2018).
6. R. Ouyang, J. X. Liu, W. X. Li, *J. Am. Chem. Soc.* **135**, 1760–1771 (2013).
7. Q. Wan *et al.*, *Nanoscale* **10**, 17893–17901 (2018).
8. E. M. Dietze, F. Abild-Pedersen, P. N. Plessow, *J. Phys. Chem. C* **122**, 26563–26569 (2018).
9. X. Yang *et al.*, *Nat. Commun.* **10**, 1611 (2019).
10. J. Zhang *et al.*, *Nat. Catal.* **1**, 540–546 (2018).
11. H. Tang *et al.*, *Sci. Adv.* **3**, e1700231 (2017).
12. T. W. van Deelen, C. Hernández Mejía, K. P. de Jong, *Nat. Catal.* **2**, 955–970 (2019).
13. Y. Y. Zhou *et al.*, *Nat. Catal.* **3**, 454–462 (2020).
14. Q. Fu *et al.*, *Science* **328**, 1141–1144 (2010).
15. J. Hulva *et al.*, *Science* **371**, 375–379 (2021).
16. S. D. Huang, C. Shang, P. L. Kang, X. J. Zhang, Z. P. Liu, *Wiley Interdiscip. Rev. Comput. Mol. Sci.* **9**, e1415 (2019).
17. H. Jeong *et al.*, *Nat. Catal.* **3**, 368–375 (2020).
18. S. L. Hu, W. X. Li, *ChemNanoMat* **4**, 510–517 (2018).
19. S. L. Hu, W.-X. Li, *Sci. China Technol. Sci.* **62**, 762–772 (2019).
20. P. Yin *et al.*, *Nat. Commun.* **12**, 4865 (2021).
21. S. L. Hemmingson, C. T. Campbell, *ACS Nano* **11**, 1196–1203 (2017).
22. M. Sterrer, T. Risse, M. Heyde, H. P. Rust, H. J. Freund, *Phys. Rev. Lett.* **98**, 206103 (2007).
23. C. T. Campbell, Z. T. Mao, *ACS Catal.* **7**, 8460–8466 (2017).
24. J. A. Farmer, C. T. Campbell, *Science* **329**, 933–936 (2010).
25. G. S. Parkinson, *Surf. Sci. Rep.* **71**, 272–365 (2016).
26. Y. Fukamori *et al.*, *ChemCatChem* **5**, 3330–3341 (2013).
27. P. Lu, C. T. Campbell, Y. Xia, *Nano Lett.* **13**, 4957–4962 (2013).
28. C. K. Lambert, *Nat. Catal.* **2**, 554–557 (2019).
29. S. L. Hu, W.-X. Li, Sabatier principle of metal-support interaction for design of ultrastable metal nanocatalysts, Zenodo (2021); https://doi.org/10.5281/zenodo.5524646.

SUPPLEMENTARY MATERIALS

science.org/doi/10.1126/science.abi9828
Materials and Methods
Supplementary Text
Figs. S1 to S33
Tables S1 to S4
References (*30–53*)
Movies S1 to S4
Data S1 to S6